Enabling Space-Based Computed Cloud Tomography with a Mixed Integer Linear Programming Scheduler

David Stanley,[*†] and Robyn Woollands,[‡ §]
University of Illinois, Urbana-Champaign, IL 61801, USA

Amir Rahmani,[¶] Federico Rossi,[‖] Changrak Choi,[**] and Anthony B. Davis[††]
Jet Propulsion Laboratory, California Institute of Technology, Pasadena, CA 91109, USA

Cumuliform clouds in Earth's lower atmosphere play important roles in the radiative balance and hydrological cycle of the climate system. Yet key processes unfolding in these clouds, such as aerosol interactions and precipitation initiation, are still poorly understood. Current space-based cloud observation methods are inadequate for inferring the internal structure of clouds outside of a narrow transect that is probed actively by radar and lidar. Cloud tomography is an emerging technique that uses passive imaging a cloud target from multiple locations with a large angular range to infer internal cloud structure. Many low convective clouds only have a lifetime of 15–25 minutes necessitating autonomous scheduling of observation targets as they appear. On-board autonomous scheduling is formulated as a mixed integer optimization problem (MILP) with a finite time horizon and a reward scheme designed to maximize the angular range of the observations. A finite time horizon MILP scheduler is well suited to this mission because the short lifetime of low convective clouds creates a natural time horizon. This MILP can solve for an optimal observation schedule in a maximum time of 15 ms on a desktop CPU. The MILP scheduler is able to observe nearly 60% more targets than a conventional push-broom camera configuration. This initial result is promising and demonstrates the need for continued research in this area.

I. Introduction

Weather and climate affect our everyday lives. The Earth is experiencing record setting weather events more rapidly than before due to climate change. From cities flooding due to tremendous rainfall, to powerful hurricanes battering

Presented at the 33rd AAS/AIAA Space Flight Mechanics Meeting on January 17, 2023 in Austin, Texas. Paper number AAS 22-336.
[*]Corresponding Author: davidms4@illinois.edu
[†]PhD Student, Department of Aerospace Engineering.
[‡]Assistant Professor, Department of Aerospace Engineering.
[§]JPL Affiliate, Jet Propulsion Laboratory.
[¶]Supervisor, Maritime and Multi-Agent Autonomy Group.
[‖]Robotics Technologist, Maritime and Multi-Agent Autonomy Group.
[**]Robotics Technologist, Maritime and Multi-Agent Autonomy Group.
[††]Scientist, Aerosol and Cloud Group.

coastal communities and wildfires encroaching on cities, we can expect unprecedented weather events to be the norm in future years. In October of 2021 The United States Department of Defense cited the increased frequency of extreme weather as a contributing factor to worldwide geopolitical instability [1]. Despite the socio-economic impact that these events can have on large populations, current forecasting tools are not adequate to predict when and where these events will occur outside of a short time frame. Our best climate models can only make generalized predictions about the qualitative changes in weather patterns, and even then, the models carry great uncertainty in the expected outcomes. Most cloud observation instruments are only able to observe the outer edges of a cloud, and thus one of the main contributors to uncertainty is in the properties of clouds and aerosols in the atmosphere [2]. In particular, feedbacks of low convective clouds over oceans are responsible for the largest amount of in inter-model climate predictions [3]. It is not well understood how strongly convection effects cloud feedback processes and whether any key processes are missing altogether in climate modeling [4]. To improve model predictions, we need more targeted campaigns to estimate jointly water vapor field structure and convectively-driven cloud properties in the lower troposphere [e.g., 5].

Cloud Tomography (CT) is an emerging passive cloud observation technique where volumetric properties of vertically-developped 3D clouds are inferred using techniques inspired by diffuse optical tomography. Current methods of remote cloud observation do not model the 3D radiation transfer (RT) unfolding in nature, which are instead represented by far simpler 1D RT models. Therein, the cloud is assumed to be a horizontally infinite plane-parallel slab. This assumption induces large errors in the retrieved properties of cumuliform clouds that have finite aspect ratios. This contributes to our poor understanding of these clouds and, in turn, to a major source of uncertainty in Earth climate models.

CT requires measurements from multiple angles to reconstruct the measured object in 3D. For CT, this necessitates either a single high-speed platform (e.g., an aircraft or a single satellite) that can image from multiple angles over time, or a network of multiple cameras (e.g., a constellation of cubesats) that can be coordinated to observe from multiple angles simultaneously. Single satellites are used for imaging clouds globally, though current observation is only done from a single viewpoint. CT has previously been demonstrated by taking cloud measurements from an airplane that flew over the target cloud [6]. However, this approach is limited both temporally and spatially, and is thus not ammenable to accurate reconstruction of large-scale clouds [7].

To fully take advantage of CT it is desirable to image the clouds from multiple viewpoints at the same time (see Figure 1). Using a single large satellite with forward and aft cameras to image an observation target has been proposed for CT [7]. The Multi-angle Imaging SpectroRadiometer (MISR) [8] aboard the Terra satellite is equipped with nine along-track sensors (referred to as "push-broom" scanners due to their sweeping push broom like motion over the ground) oriented between 70.5 degrees fore and aft. Each sensor operates by successively imaging thin strips of the Earth along Terra's ground track. Each strip is joined together to create an image that is approximately 400 km wide by 20,000 km long for every orbit. MISR/Terra images a single observation target from multiple angles over a period of roughly seven

minutes. However, as previously mentioned, this technique introduces errors in the 3D cloud reconstruction due to the temporal variability of cloud structure, even over short time scales. To eliminate these errors all the observations for a single CT reconstruction must be performed at the same time. This necessitates a system of multiple satellites (swarm) that can autonomously coordinate with each other in real-time to observe the same observation target at the same time from multiple angles [9, 10].

Autonomous operations of satellites is now routine in space missions and has been successfully demonstrated by teams like ECOSTRESS, which made use of autonomy scheduling to mitigate the platform's limited storage and downlink capacity for Earth observations [11]. Distributed autonomy of multiple satellites operating and coordinating as a distributed sensor is only just beginning to be tested in space with V-R3X launched in early 2021 [12], but it is gaining great interest for many Earth observing missions, such as for estimating bidirectional-reflectance [13, 14], and performing multi-payload (multi-instrument) observation missions[15][16]. In addition, distributed autonomy has also been considered for mission concepts at Mars. Woollands et al. [17] recently proposed an autonomous satellite swarm to survey Mars' surface for dust devils that could automatically re-task agents in the swarm to take as many follow-up images as possible to study how the dust devils evolve over time. Autonomous follow-up and simultaneous imaging are two of the key advantages for an agile swarm over conventional techniques like passive along-track or cross-track scanning with a single multi-sensor satellite.

In this paper, we simulate a swarm of cubesats with agile pointing capability that can autonomously and remotely collect images of clouds in the lower atmosphere from orbit. Camera pointing requirements are determined in real-time using mixed integer linear programming (MILP). MILP has been shown to be an effective method for calculating optimal observation schedules for planetary observing satellites when the search space is too large to be fully traversed [18][17]. The measurement process and performing the cloud reconstruction using CT is beyond the scope of this paper. We refer the interested reader to Castro et al. [19] for a multi-angle approach to reconstruction of a cloud's outer shape and to Tzabari et al. [10] for the design of a multi-cubesat implementation of CT. In its present status, CT is limited to relatively modest clouds (a few km in size) observed at high spatial resolution (pixels are $\sim$10s of meters) whether from airborne or space-based sensors [7]. Large clouds are thus not yet targets for CT, whether they are of the cumuliform or of the stratiform types.

That said, the present study does assume that the relatively small cumulus clouds of interest can be detected in each image and then identified as targets across the multi-view images. This problem was solved long ago using basic image "feature" identification that enables MISR's cloud top height [20] and cloud-traced horizontal wind vector [21] products. These algorithms have been adapted from MISR's relatively large (275 m) pixels to their much smaller counterparts (e.g., from airborne sensors) used currently in CT. We will assume in the present study that such cloud detection-and-tracking has been implemented in the onboard processing, which is well within current technological capability.

The remainder of the paper is organized as follows. The cloud model and preprocessing is discussed in the following

section. This is followed by a section detailing the orbits and camera specifications. The MILP problem formulation for the autonomous scheduling of observations is presented next, followed by a section detailing the push-broom camera configuration that we used as a baseline to compare the MILP results. Finally, the results and conclusion are presented respectively in Sections VI and VII.

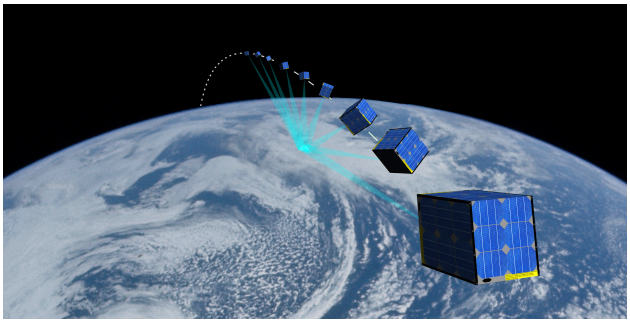

Fig. 1 Coordinated Cubesat Swarm Imaging a Cloud

II. Cloud Model & Preprocessing

In this study, we adopt a simple *random model* for cloud target generation. These cloud targets are represented for each observation opportunity by points in the lower troposphere, which is where convective cloud systems are likely to occur. Since observations are only possible in areas illuminated by the Sun, our cloud model takes this into account to save computation time (i.e., no clouds simulated during the night). We center the clouded region at 1:30 pm local solar time. Over this region, the cloud targets are simulated with an average density of one per ten square kilometers with a mean lifetime of 21.6 minutes on average [22, 23]. Formation and dissipation times are computed for each target. We have not taken into account the velocity of the clouds in the atmosphere as we are primarily interested in simultaneous measurements at a single time rather than multiple follow-up measurements and for our chosen swarm geometry (see the following section). The time between repeat ground tracks is on the order of days, which far exceeds the lifetime of the clouds of interest in this study. Although this is a low-fidelity global cloud distribution model, it is adequate to test the performance of our on-board scheduler.

A. Swarm Field of View

For the MILP to function, the algorithm must know what areas of the Earth the satellite swarm is capable of imaging during each time step. Each satellite in the swarm is equipped with a 1.47° boresight camera and agile pointing capabilities. It is assumed that each satellite is capable of pointing anywhere between its nadir and the local horizon. This pointing range is shown at various latitudes in Figure 2. These areas are defined by the intersection of a sphere with the radius of the Earth, R_{eq} and cones with apexes centered on each satellite and axes pointing towards the center of the Earth (nadir). Each cones' half-angle is equal to the angle between the nadir vector and a line passing through the

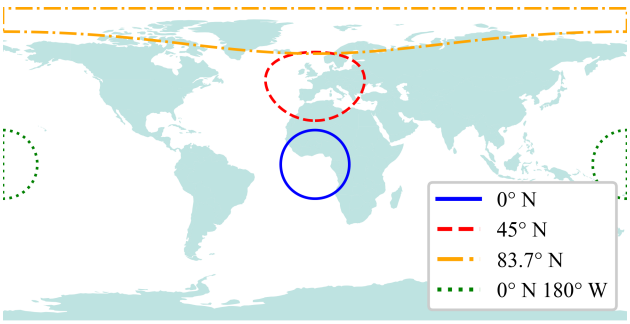

Fig. 2 Projected viewing horizons for a satellite at 400 km altitude at different latitudes.

cone's apex and a point tangent to the Earth sphere. The formulation by I. Ruff was used to calculate the FOV ground boundaries in latitude and longitude coordinates [24]. The swarm FOVs appear as a line of overlapping circles along the orbital ground track. The viewable area for the swarm (i.e. the field of regard for the swarm) is the ground area that is viewable by all nine satellites simultaneously. Conveniently this area is equal to the intersection of the most forward and most aft satellites' conical FOVs. This intersection forms a lens shape on the ground as seen n figure 3. If this lens area exists, then every satellite in between these two bounding satellites must contain this lens area in their own field of view. The viewable area is calculated at each time step and stored as a series of coordinates (lon, lat) that define the boundary. In the case of the viewable area intersecting the antimeridian, the viewable area is stored as two strings of coordinates defining the area covered on each side of the line.

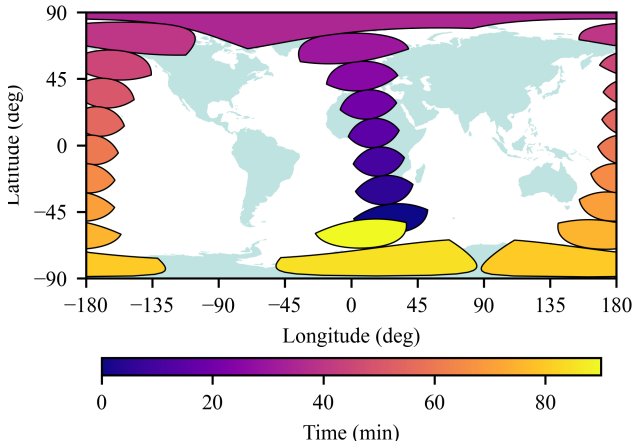

Fig. 3 The lens shaped field of regard of the swarm is projected onto a rectilinear map of Earth's surface in five minute intervals over one orbit

B. Cloud Data Pruning

Because of the constraints that any observation opportunity must be illuminated by the Sun, and that the convectively-driven clouds of interest will mostly exist between 60° N/S latitude, the swarm will spend more than half of each orbit without any suitable observation targets within the viewable area. This conveniently provides a naturally occurring

planning time-horizon, but also means that large segments of time will contain configurations without any solution. To filter out these time ranges the raw cloud data from the numerical cloud simulation is imported into Python as a Pandas data frame. Each observation opportunity is stored in the data frame as a row with the target's start time, end time, latitude and longitude. A second data frame that will be fed to the MILP is created where each row corresponds to a single time step. The rows contain the time in seconds, the coordinates for every observation opportunity that currently exists, the swarm's viewable area, the positions of the satellites, the viewable observation opportunity, the observation angular range for each viewable opportunity, and a count of viewable opportunities. The steps for generating a row of the input data for each time step are as follows:

1) Get the current time, t
2) Query the raw cloud data frame to find all observation opportunities with start times earlier than the current time. $t_{start} \leq t$.
3) Query the opportunity data retrieved in the previous step for all opportunities with end times later than the current time. $t_{end} \geq t$. Store this as the opportunities that currently exist at t, $C(t)$.
4) Retrieve the viewable area for the swarm at t, $A(t)$.
5) Calculate the intersection of the existing opportunities with the viewable area.

$$V(t) = C(t) \cap A(t)$$

6) Calculate the angular observation range for each viewable opportunity, $N(c,t)$.

$$N(c,t) = \begin{cases} angularRange(c,t), & \text{if } c \in V(t) \\ 0, & \text{otherwise} \end{cases} \tag{1}$$

7) Store the count of observable opportunities, $length(V(t))$

For each row where the count of observable opportunities is 0, remove the row.

III. Orbit & Cameras

For this simulation a circular inclined orbit is simulated for the swarm of nine cubesats. The swarm is in a low Earth orbit (400km altitude). The chief satellite is located in the center of the swarm. The eight deputy satellites are located in the same orbit with the only difference being that their arguments of latitude are offset from the chief to form a string of pearls (or train) configuration. The argument of latitude offsets for the satellites from most forward to most-aft are {10, 7.5, 5.0, 2.5, 0.0, -2.5, -5.0, -7.5, -10.0} degrees. The only perturbation included in the orbit simulation is the Earth's dominant zonal harmonic, J_2 gravity perturbation, that is caused by the Earth's oblateness. Figure 4 demonstrates how

the ground track of the Sun synchronous orbit follows the movement of the illuminated clouds every orbit. The orbit does not have an exact ground track revisit period, but the swarm will approximately repeat the original ground track after two days or thirty one complete orbits.

We have selected a low Earth orbit such that the cubesat camera (for example, KAI-04050 2336 (H) $\times$ (V) Interline) is capable of imaging the clouds with a resolution of less than 10 m with a 250 mm lens and less than 5 m with a 500 mm lens [25]. A Sun synchronous orbit is chosen to ensure that the lighting conditions (shadow angles and shadow lengths) are similar for every pass. Although we do not simulate cloud detection through image processing in this paper, we assume that using the same lighting conditions for each pass will aid the eventual cloud detection algorithm, thus reducing the potential for false positives. Each cubesat camera has a field of view with 1.47° boresight angle.

IV. MILP Problem Formulation

In the section, we present the methodology for autonomously scheduling camera pointing so as to the maximize the number of simultaneous observations of each observation opportunity. We assume that the formation of clouds in the Earth's atmosphere occurs stochastically and with a known temporal and spatial distribution, and that these clouds dissipate within a maximum time window of 25 minutes. We assume a constellation of cubesats observing lower tropospheric clouds from low-Earth-orbit using onboard cameras with agile pointing capabilities. The orbits are fixed, however each spacecraft can decide where to point its camera. For the selected string of pearls configuration, adjacent spacecraft always have a line-of-sight communication link, thus permitting agents to share information regarding the time and location of observation opportunities with each other.

The goal is to maximize the number of simultaneous observations of each observation opportunity, specifically, we assume it is more valuable to collect multiple observations of the same target over a wide range of viewing angles, rather than to collect time spaced (follow-on) observations of the same target.

A. Receding-horizon Approach

Obtaining a solution to the above problem requires knowledge of the observation opportunities. Thus, the problem should be solved again as new targets are observed. To address this, the algorithm is implemented in a receding horizon manner. In our simulation, we use a time horizon of 22 minutes as this is how long it takes for one flyover of the illuminated cloud cluster. Each MILP solution takes on average 4.4 ms to compute. As soon as new cloud observation information is available, the problem is re-solved over the same time horizon (i.e. the 22 minutes following the update). Before the horizon is reached, the problem is solved again even if no new information is available.

Solving an MILP for satellite planning with many constraints over a long period of time is computationally expensive. Decisions made at an earlier time step may greatly effect the decisions made during a later time step due to constraints on slewing rate and power. By creating a receding time horizon where the MILP only finds an optimal solution up to an

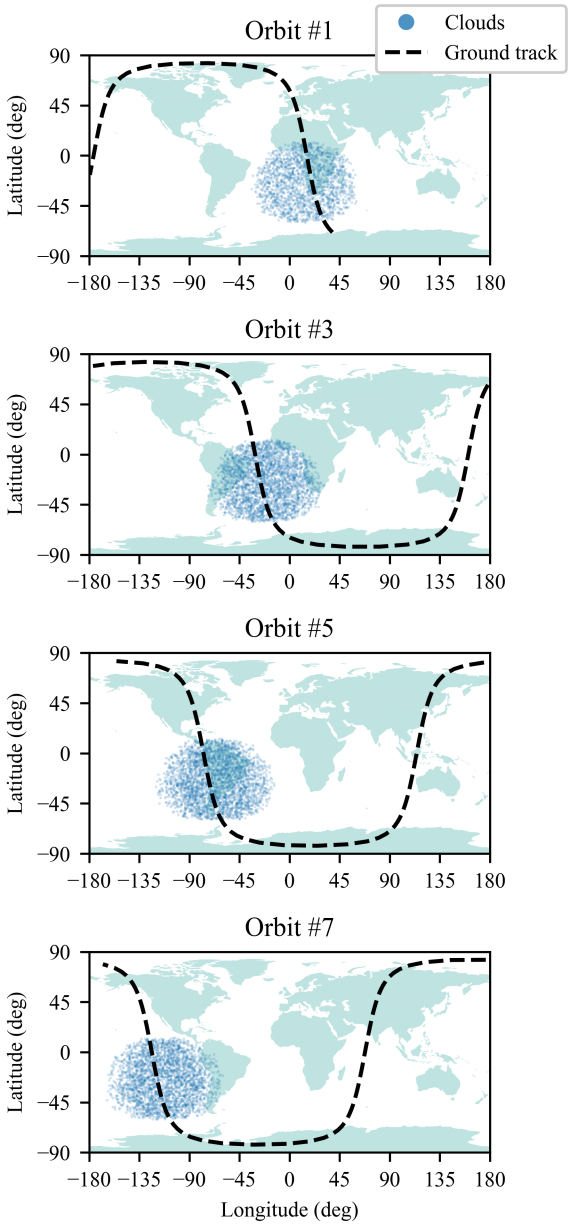

Fig. 4 Multiple Orbit Flyovers

arbitrary time, the computational time may be suitably bounded. The downside to this approach is that if later decisions are strongly coupled to previous states, then the MILP will not necessarily find an optimal solution for the entire time span. For computed cloud tomography there is a limited time frame during which the swarm will be flying over a group of suitable targets because the satellite swarm relies on solar radiation for illuminating their observation opportunities. During the night side of the orbit, the swarm can divert resources to down linking observations and preparing for the next illuminated overpass. This means that pointing decisions made by the MILP in a later orbit are uncoupled from pointing decisions made during an earlier orbit. Therefore the receding time horizon should be chosen to be the amount of time it takes for the satellite to pass over the group of daylight illuminated cloud targets.

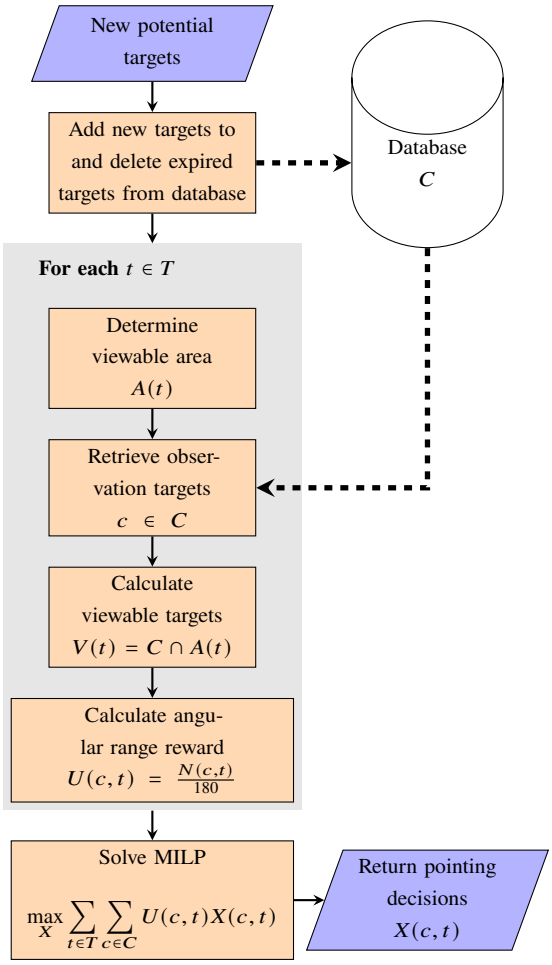

Fig. 5 The process of maintaining a database of possible observation opportunities with steps for preparing inputs for the MILP scheduling problem

The process to prepare the inputs for the MILP is show in figure 5 and described in detail below. To formulate the ILP we must first define a number of variables.

- T, a planning time horizon that begins at t_1 and ends at t_M.
- C, a set of cloud observation opportunities c that exist and may be viewable during the time horizon T.

- $V(c,t)$, a set of boolean values where each value is 1 iff a cloud observation opportunity $c \in C$ is within the swarm's FOV $A(t)$ at time $t \in T$.
- $X(c,t)$, a set of boolean decision variables where each value is 1 iff a cloud observation opportunity $c \in C$ is pointed at by the swarm at time $t \in T$. The pointing variable.
- $U(c,t)$, a set of float values (0,1) than are calculated based on the angular range of observations for cloud observation opportunity $c \in C$ at time $t \in T$. The reward function.
- $N(c,t)$, a set of float values (0,180) where each value is equal to the angle in degrees made between the most forward satellite's position, the cloud observation opportunity $c \in C$'s position and the most aft satellite's position at time $t \in T$. This value is highest when a target is imaged directly below the geometric center of the swarm.

We are now in a position to define the constellation CT problem as an ILP as follows:

$$\max_{X} \sum_{t \in T} \sum_{c \in C} U(c,t) X(c,t) \tag{2}$$

subject to the constraints

$$\sum_{c \in C} X(c,t) \leq 1 \qquad \forall t \in T \tag{3}$$

$$X(c,t) \leq V(c,t) \qquad \forall c \in C, t \in T \tag{4}$$

and with reward function

$$U(c,t) = \frac{1}{180} N(c,t) \tag{5}$$

Equation (2) is the objective function that must be maximized with respect to the decision variable X. The objective being a reward based on the reward of each observed cloud target. U is the reward function, but because the decision variable X is boolean, the reward may only be gained if X is one. Equation (3) guarantees that the swarm may only target at most one observation opportunity per time step. Equation (4) guarantees that only opportunities that are viewable may be targeted at time t. Equation (5) is the reward function which is based on the angular range of observing an observation opportunity at time t. Because the angular range may span (0,180) the reward value is equal to 180^{th} of the angular range and may span (0,1). The MILP is solved for each time horizon using IBM's CPLEX solver (V22.1)[26].

V. Baseline Push broom Swarm

A. Push-broom Field-of-View

In this paper we compare our method for obtaining observations with the well known push broom method. We consider nine hypothetical satellites each equipped with a push broom scanner in the same orbital formation as our proposed mission: nine 400 km altitude Sun synchronous orbits that are each separated by 2.5 degrees in the argument of latitude. The scanners for each satellite are oriented such that they image the lower atmosphere directly nadir to the central chief satellite. This allows simultaneous imaging from nine different angles. For our simulation, we assume that the push broom scanner has a cross-track field-of-view (FOV) of 28.6° and constantly images a 204 km swath along the satellite's ground track, which is similar to swath width that NASA's MISR sensor on board the Terra satellite would have at an altitude of 400 km.

For reference, the Terra satellite, launched in 1998, orbits at an altitude of about 705 km and has a cross track field of view of 29.8 degrees providing a ground swath width of about 400 km and a minimum spatial resolution of 150 m [8]. Landsat 9, launched in 2021, orbits at an altitude of 705 km and has a push-broom sensor (OLI-2) swath width of 185 km [27]. Landsat 9 has a spatial resolution of 15 m to 30 m depending on the spatial band. This is comparable to our system's chosen spatial resolution of 10 m. We chose our hypothetical baseline to have a similar FOV to the MISR on Terra and the spatial resolution of a modern push broom scanner to provide a challenging comparison to our method. Terra's FOV was specifically chosen, because images from MISR on Terra have been targeted as a potential source of data for CT due to the instrument's nine viewing angles [7].

We assume that the swath imaged by the push-broom system is discretized into four second regions which leads to rectangular polygons used for cloud detection. It is possible that multiple clouds occur simultaneously in the same swath region. In comparison to the autonomous swarm with arbitrarily pointing capabilities, the push broom formation is unable to arbitrarily point, and its field of regard, the region where it can detect clouds is much smaller at 204 km wide. Conversely, the push-broom always captures the entire 204 km swath, whereas the autonomous swarm only has a ground vertical FOV of about 7.5 km with a 500 mm focal length. So, the swarm is only ever able to capture a small region within its slewing range at each time step. Figure 6 graphically compares these areas relative to each other.

VI. Results

A. MILP Scheduling

For the chosen orbit and cloud model, each flyover of the swarm lasted 21-23 minutes. The variation in flyover time is caused by the time horizon discretization and the fact that clouds are not guaranteed to be present within the swarm FOV as the spacecraft approaches the region of interest. Pre-processing of cloud data would automatically discard these empty time steps to reduce computation time. The MILP scheduler was run for 7 consecutive flyovers of the region of

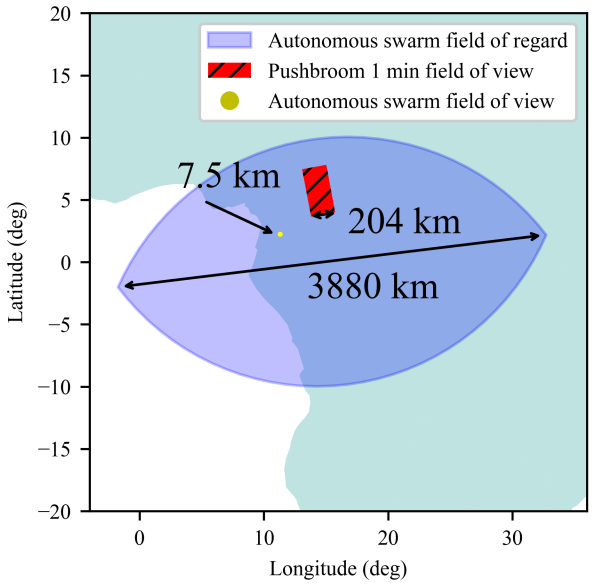

Fig. 6 Push-broom scanning swath over one minute compared to swarm slewing range for one time step and the instantaneous FOV for a camera in the swarm.

interest. Each solution took an average of 4.4 ms with a maximum solve time of 15.9 ms on an AMD Ryzen 5 2600. The MILP successfully targeted one cloud per time step with a total count of 161 clouds being imaged. The average angular range of observation was 148.1 degrees. The distribution of observation angular ranges is shown in Figure 7. Compared with our MILP scheduled pointing swarm, the push broom approach captured 101 clouds with an average angular range of 153.1 degrees. This is higher than the MILP average, because the push broom swarm was configured to only image below the center of the swarm where the angular range is greatest. Figure 7 shows the distribution of recorded angular ranges. The baseline configuration captures more clouds between 155° and 160° due to its ability to image multiple clouds in one time step. As the angular range decreases the observation targets fall outside of the pushbroom scanners'

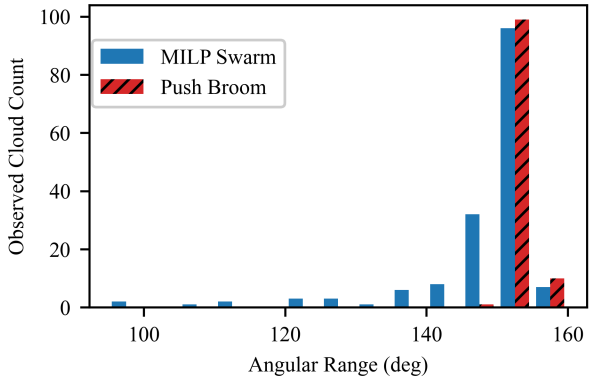

Fig. 7 Observation count distribution binned by angular range in 5° intervals

FOV and are unable to be imaged. In comparison, the MILP swarm is capable of imaging clouds much further from the geometric center. Overall, the MILP scheduled agile pointing swarm captured 59.4% more clouds than the push broom baseline configuration. This is a promising result and demonstrates the need for continued research and development in support of autonomous remote sensing swarm missions.

VII. Conclusion

This paper is a preliminary analysis of utilizing autonomous scheduling to effectively choose observation targets that are randomly distributed over the Earth. In particular, the on-board scheduler is used to maximize the number of simultaneous observations of cloud to enable future on-orbit cloud tomography missions. The on-board autonomous scheduler is formulated as a mixed integer optimization problem (MILP) with a finite time horizon and a reward scheme designed to maximize the angular range of the observations. This MILP can solve for an optimal observation schedule in a maximum time of 15 ms on a conventional desktop CPU. The MILP scheduler is able to select 59.4% more targets than a conventional push broom camera configuration. This initial result is promising and demonstrates the need for continued research efforts in this area.

VIII. Acknowledgments

This work was carried out at the University of Illinois, Urbana-Champaign, as well as during a summer internship at the Jet Propulsion Laboratory, California Institute of Technology, under contract with the National Aeronautics and Space Administration (80NM0018D0004). The work was funded by the JPL Spontaneous Research and Technology Development Program. We thank the anonymous reviewers for their incisive comments that helped us improve the paper during its revision.

References

[1] DoD, "Department of Defense Climate Risk Analysis," 2021. URL https://media.defense.gov/2021/Oct/21/2002877353/-1/-1/0/DOD-CLIMATE-RISK-ANALYSIS-FINAL.PDF.

[2] Boucher, O., Randall, P. A. D., Bretherton, C., Feingold, G., Forster, P., Kerminen, V.-M., Kondo, Y., Liao, H., Lohmann, U., Rasch, P., Satheesh, S., Sherwood, S., Stevens, B., and Zhang, A. X., "2013: Clouds and aerosols," *Climate Change 2013: The Physical Science Basis*, 2013, pp. 571–657. https://doi.org/10.1017/cbo9781107415324.016.

[3] Sherwood, S. C., Bony, S., and Dufresne, J.-L., "Spread in model climate sensitivity traced to atmospheric convective mixing," *Nature*, Vol. 505, No. 7481, 2014, pp. 37–42. https://doi.org/10.1038/nature12829.

[4] Bony, S., Stevens, B., Frierson, D. M. W., Jakob, C., Kageyama, M., Pincus, R., Shepherd, T. G., Sherwood, S. C., Siebesma, A. P., Sobel, A. H., Watanabe, M., and Webb, M. J., "Clouds, circulation and climate sensitivity," *Nature Geoscience*, Vol. 8, No. 4, 2015, pp. 261–268. https://doi.org/10.1038/ngeo2398.

[5] Dandini, P., Cornet, C., Binet, R., Fenouil, L., Holodovsky, V., Schechner, Y. Y., Ricard, D., and Rosenfeld, D., "3D cloud envelope and cloud development velocity from simulated cloud (C3IEL) stereo images," *Atmospheric Measurement Techniques*, Vol. 15, No. 20, 2022, pp. 6221–6242. https://doi.org/10.5194/amt-15-6221-2022, URL https://amt.copernicus.org/articles/15/6221/2022/.

[6] Levis, A., Schechner, Y., A., A., and Davis, A. B., "Airborne Three-Dimensional Cloud Tomography," *IEEE International Conference on Computer Vision (ICCV)*, 2015. https://doi.org/10.1109/ICCV.2015.386.

[7] Forster, L., Davis, A. B., Diner, D. J., and Mayer, B., "Toward Cloud Tomography from Space Using MISR and MODIS: Locating the "Veiled Core" in Opaque Convective Clouds," *Journal of the Atmospheric Sciences*, Vol. 78, No. 1, 2021, p. 155–166. https://doi.org/10.1175/jas-d-19-0262.1.

[8] NASA, "MISR: Multi-angle Imaging SpectroRadiometer," https://misr.jpl.nasa.gov/mission/misr-instrument/, n.d. Accessed: 2022-29-07.

[9] Schilling, K., Yoav, Y. S., and Ilan, K., "CloudCT – Computed Tomography of Clouds by a Small Satellite Formation," *12th IAA symposium on Small Satellites for Earth Observation*, 2019.

[10] Tzabari, M., Holodovsky, V., Shubi, O., Eytan, E., Altaratz, O., Koren, I., Aumann, A., Schilling, K., and Schechner, Y. Y., "CloudCT 3D volumetric tomography: Considerations for imager preference, comparing visible light, short-wave infrared, and polarized imagers," *Polarization Science and Remote Sensing X*, Vol. 11833, SPIE, 2021, pp. 19–26. https://doi.org/10.1117/12.2594134.

[11] Yelamanchili, A., Chien, S., Moy, A., Shao, E., Trowbridge, M., Cawse-Nicholson, K., Padams, J., and Freeborn, D., "Automated Science Scheduling for the ECOSTRESS Mission," *International Workshop for Planning and Scheduling for Space (IWPSS 2019)*, 2019, pp. 204–211. URL https://ai.jpl.nasa.gov/public/documents/papers/yelamanchili-iwpss2019-ecostress-scheduling.pdf.

[12] Trenberth, K. E., Fasullo, J. T., and Kiehl, J., "Earth's Global Energy Budget," *Bulletin of the American Meteorological Society*, Vol. 90(3), 2009, pp. 311–324. https://doi.org/10.1175/2008BAMS2634.1.

[13] Nag, S., Gatebe, C. K., and Weck, O. D., "Observing system simulations for small satellite formations estimating bidirectional reflectance," *International Journal of Applied Earth Observation and Geoinformation*, Vol. 43, 2015, pp. 102–118. https://doi.org/10.1016/j.jag.2015.04.022.

[14] Monmousseau, P., "Scheduling of a Constellation of Satellites: Creating a Mixed-Integer Linear Model," *Journal of Optimization Theory and Applications*, Vol. 191, No. 2–3, 2021, p. 846–873. https://doi.org/10.1007/s10957-021-01875-2, URL http://dx.doi.org/10.1007/s10957-021-01875-2.

[15] Levinson, R., Nag, S., and Ravindra, V., "Agile Satellite Planning for Multi-Payload Observations for Earth Science," 2021. https://doi.org/10.48550/ARXIV.2111.07042, URL https://arxiv.org/abs/2111.07042.

[16] Levinson, R., Niemoeller, S., Nag, S., and Ravindra, V., "Planning Satellite Swarm Measurements for Earth Science Models: Comparing Constraint Processing and MILP Methods," *Proceedings of the International Conference on Automated Planning and Scheduling*, Vol. 32, No. 1, 2022, pp. 471–479. https://doi.org/10.1609/icaps.v32i1.19833, URL https://ojs.aaai.org/index.php/ICAPS/article/view/19833.

[17] Woollands, R., Rossi, F., Stegun Vaquero, T., Sanchez Net, M., Bae, S. S., Bickel, V., and Vander Hook, J., "Maximizing Dust Devil Follow-Up Observations on Mars Using Cubesats and On-Board Scheduling," *The Journal of the Astronautical Sciences*, Vol. 69, No. 3, 2022, p. 918–940. https://doi.org/10.1007/s40295-022-00317-z, URL http://dx.doi.org/10.1007/s40295-022-00317-z.

[18] Chen, X., Reinelt, G., Dai, G., and Spitz, A., "A mixed integer linear programming model for multi-satellite scheduling," *European Journal of Operational Research*, Vol. 275, No. 2, 2019, p. 694–707. https://doi.org/10.1016/j.ejor.2018.11.058, URL http://dx.doi.org/10.1016/j.ejor.2018.11.058.

[19] Castro, E., Ishida, T., Takahashi, Y., Kubota, H., Perez, G. J., and Marciano, J. S., "Determination of Cloud-top Height through Three-dimensional Cloud Reconstruction using DIWATA-1 Data," *Scientific Reports*, Vol. 10, No. 1, 2020. https://doi.org/10.1038/s41598-020-64274-z, URL http://dx.doi.org/10.1038/s41598-020-64274-z.

[20] Moroney, C., Davies, R., and Muller, J.-P., "Operational retrieval of cloud-top heights using MISR data," *IEEE Transactions on Geoscience and Remote Sensing*, Vol. 40, No. 7, 2002, p. 1532–1540. https://doi.org/10.1109/tgrs.2002.801150, URL http://dx.doi.org/10.1109/tgrs.2002.801150.

[21] Horváth, A., and Davies, R., "Feasibility and Error Analysis of Cloud Motion Wind Extraction from Near-Simultaneous Multiangle MISR Measurements," *Journal of Atmospheric and Oceanic Technology*, Vol. 18, No. 4, 2001, p. 591–608. https://doi.org/10.1175/1520-0426(2001)018<0591:faeaoc>2.0.co;2, URL http://dx.doi.org/10.1175/1520-0426(2001)018<0591:faeaoc>2.0.co;2.

[22] Zhao, M., and Austin, P. H., "Life Cycle of Numerically Simulated Shallow Cumulus Clouds. Part I: Transport," *Journal of the Atmospheric Sciences*, Vol. 62, No. 5, 2005, p. 1269–1290. https://doi.org/10.1175/jas3414.1, URL http://dx.doi.org/10.1175/jas3414.1.

[23] King, M. D., Platnick, S., Menzel, W. P., Ackerman, S. A., and Hubanks, P. A., "Spatial and Temporal Distribution of Clouds Observed by MODIS Onboard the Terra and Aqua Satellites," *IEEE Transactions on Geoscience and Remote Sensing*, Vol. 51, No. 7, 2013, p. 3826–3852. https://doi.org/10.1109/tgrs.2012.2227333, URL http://dx.doi.org/10.1109/tgrs.2012.2227333.

[24] Ruff, I., "The intersection of a cone and a sphere: A contribution to the geometry of satellite viewing," *Journal of Applied Meteorology*, Vol. 10, No. 3, 1971, p. 607–609. https://doi.org/10.1175/1520-0450(1971)010<0607:tioaca>2.0.co;2.

[25] *KAI-04050 2336 (H) x 1752 (V) Interline CCD Image Sensor*, ON Semiconductors, 2 2017. URL https://www.mouser.com/datasheet/2/308/KAI-04050-D-1810344.pdf, rev. 6.

[26] CPLEX, I. I., "V22.1: User's Manual for CPLEX," *International Business Machines Corporation*, 2022. URL https://www.ibm.com/docs/en/icos/22.1.1?topic=optimizers-users-manual-cplex.

[27] USGS, "Landsat 9," https://pubs.er.usgs.gov/publication/fs20193008, Apr 2019. Accessed: 2022-29-07.